LANGMUIR

Article

pubs.acs.org/Langmuir

Geometry-Dependent Drying in Dead-End Nanochannels

Quan Xie, Siyang Xiao, and Chuanhua Duan*

Department of Mechanical Engineering, Boston University, Boston, Massachusetts 02215, United States

Supporting Information

ABSTRACT: Liquid drying in nanoporous media is a key process in food, textile, oil and energy industries, but the corresponding kinetics remains poorly understood due to the structural complexity of nanoporous media. Here, we directly observe the drying process and study drying kinetics in single two-dimensional (2-D) nanochannels with height ranging from 29 to 122 nm. Two different drying behaviors are discovered in such nanoconfinements: continuous meniscus receding and discontinuous meniscus receding due to liquid bridge formation ahead of the meniscus, albeit similar drying rates. The geometry dependence of the measured drying rates is studied at different humidities and compared with a theoretical model considering liquid corner flow, liquid thin film flow, and vapor diffusion as contributors to the overall drying rates. Individual contributions from vapor and liquid transport inside the nanochannels to the drying kinetics are decoupled, and the water vapor diffusivity is successfully extracted. Our results show that both corner flow and vapor diffusion play important roles on water drying in nanochannels without sharp corners. Our findings further indicate that water vapor diffusion in nanoscale confinements can still be described by the classic Knudsen diffusion theory. These results provide new insights of liquid drying in nanoporous media and have implication in optimizing drying processes in industrial applications.

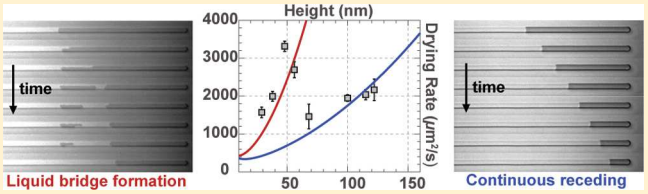

INTRODUCTION

Drying in nanoporous structures is a process related to a variety of important industrial applications including oil recovery, soil remediation, evaporative cooling, food/textile preparation and water management in fuel cell.[1,2] Previous studies focused on nanoporous media have observed drying rates significantly higher than the theoretical predications of pure vapor diffusion.[3−6] Although liquid flow has been attributed to such fast drying in porous structures,[5,7,8] the quantitative contributions and detailed kinetics remains unclear. Furthermore, recent studies on vapor transport in carbon nanotube arrays reveal that the vapor diffusion inside the nanoconduits can also be enhanced due to the wall-slip of smooth inner surfaces.[9,10] Therefore, fundamental understanding of the drying kinetics in the nanoporous structures is still needed. However, the complicated nature of nanoporous structures, including interconnected nanoscale conduits and the wide distribution of conduits sizes, makes it difficult to quantitatively study fundamental drying kinetics. One way to address this issue is to create individual nanoconduits with simple and deterministic structures (e.g., nanochannels), and then observe and study drying kinetics in such nanoconduits.

Thanks to the rapid development of micro/nanofabrication techniques, 2-D planar nanochannels with well-defined geometry has been successfully fabricated using top-down methods.[11] The capability of integration with other micro/nanofluidic components and direct observation make these nanochannels the ideal structures for many fundamental studies of mass transport and phase-change phenomena in nanoconfinement, including surface-charge-governed ion transport,[12−14] ionic current rectification,[15−17] evaporation induced cavitation,[18] capillary condensation,[19] etc. Yet, there have only been limited works that used these nanochannels to investigate drying kinetics.[20,21] Eijkel et al. discovered fast drying in nanochannels[20] and attributed the fast drying to strong liquid corner flow since its contribution (based on theoretical calculation) is 1 order of magnitude higher than other mechanisms such as liquid film flow and vapor diffusion. However, they only focused their studies in channels with sharp corners and with a height of 72 nm. Consequently, the quantitative contributions of all three aforementioned mechanisms, i.e., corner flow, thin film flow and vapor diffusion in other types of channels (e.g., channels without sharp corners) and the effect of nanoconfinement on these three mechanisms have yet to be experimentally investigated.

In this work, we systematically studied drying kinetics in nanochannels with different channel heights ranging from 29 to 122 nm and quantified the individual contributions of the aforementioned three mechanisms as a function of the channel height. Water is chosen as the drying liquid due to its significance in drying-related industrial applications.[1,2] We observed two different drying modes in these nanochannels, i.e., continuous meniscus receding and discontinuous meniscus receding, and discovered that the drying modes would not affect the overall drying rates. Our results further confirm that corner flow and thin film flow can be well described by expressions derived from continuum theories while vapor

Received: June 14, 2017
Revised: July 26, 2017
Published: July 27, 2017

DOI: 10.1021/acs.langmuir.7b02027
Langmuir 2017, 33, 8395−8403

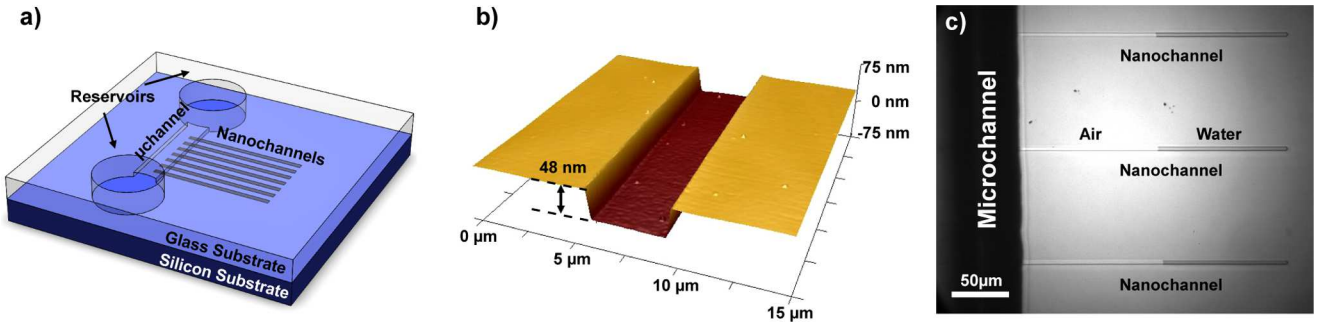

Figure 1. Schematic and characterization of the nanofluidic device for drying study. (a) Schematic of the bonded nanofluidic device. (b) Surface profile of open nanochannel (48 nm high) characterized by AFM. (c) Microscope image of the device during the drying experiment.

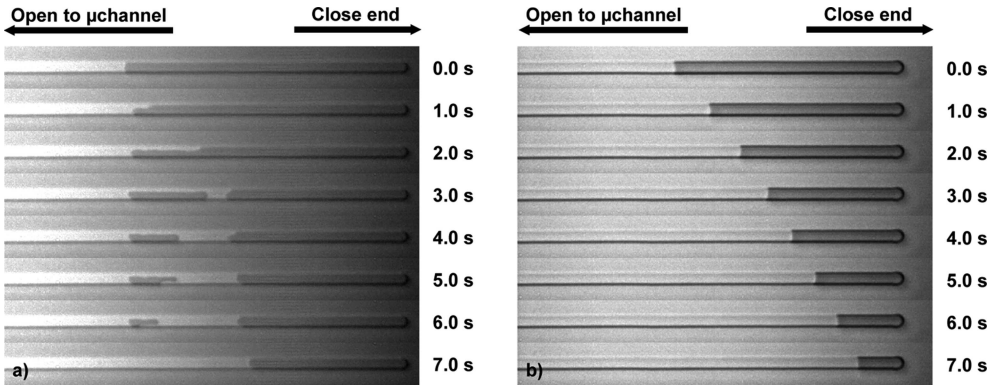

Figure 2. Microscope snapshots of drying nanochannels. (a) Snapshots of drying of 56 nm high nanochannel. (b) Snapshots of drying of 115 nm high nanochannel.

diffusion does not deviate much from the Knudsen diffusion theory.

RESULTS AND DISCUSSION

The nanochannels we used for this study are open at one end and closed at the other end. This dead-end design ensures that the liquid/vapor transport inside nanochannel is unidirectional and completely avoids the complexity in nanochannels with two open ends capillary flow could occur due to slight difference in channel height and surface properties, resulting in different meniscus receding speeds at both ends during drying. In addition, the drying process inside the dead-end nanochannels is slower than open-end nanochannels, allowing longer observation time and more accurate analysis.

Figure 1a presents a schematic of our dead-end nanochannel device. This device is composed of two substrates: glass substrate and silicon substrate. The silicon substrate has 30 open parallel nanochannels (only seven nanochannels were drawn in the schematic). The geometry of channel (L: 1000 μm; W: 3 μm; H: 29−122 nm) was well by photolithography and controlled reactive ion etching. After nanochannels being etched, 300 nm-thick silicon oxide was thermally grown onto the silicon substrate to ensure the hydrophilicity of nanochannel. Due to the conformal silicon oxide growth, the geometry of nanochannels was well preserved after the oxidation process (see Supporting Information). The glass substrate has two open reservoirs and one bridging microchannel for liquid introduction. The two substrates were brought together after fabrication and permanent enclosure of the nanochannels is formed via anodic bonding. It is worth noting that the 30 enclosed nanochannels on the same substrate have the same height and different heights of nanochannel were fabricated on different substrates. The height of the nanochannels for each device was characterized by atomic force microscopy before anodic bonding and Figure 1b shows a typical result of 48 nm-high nanochannel. After anodic bonding, the microchannel in glass substrate is only in contact with one end of our nanochannel. Therefore, the liquid introduction and removal can only happen at the open end of a nanochannel. Figure 1c shows the microscope image of our final device. Water is introduced into the nanochannel for better illustration.

Before investigating water drying in the dead-end nanochannels, oxygen plasma was applied to the nanochannel device to ensure hydrophilicity. DI water was then introduced into the dead-end nanochannel through the reservoir. The entire microchannel and a major portion of the nanochannel were filled by water within a few seconds as a result of capillary filling, while a small amount of air was quickly compressed and trapped at the dead end of nanochannel. The air trapped inside the nanochannel was slowly dissolved into the filled water column. Generally, water would completely fill the dead-end nanochannel within 10 min. Before running drying experiment, the dead end of the nanochannel was carefully checked to make sure no trapped air bubbles can be seen under microscope.

The drying process was initiated by purging dry nitrogen gas into the microchannel. The DI water in the microchannel was first blown away by high-speed nitrogen flow. Then the water meniscus formed at the intersection between nanochannel and microchannel and water inside the nanochannel started to evaporate. The meniscus moved further into the nanochannel as more water evaporated (Figure 1c). The high-speed nitrogen flow was maintained through the whole drying process until the meniscus receded to the dead end of nanochannel. To track the

DOI: 10.1021/acs.langmuir.7b02027
Langmuir 2017, 33, 8395−8403

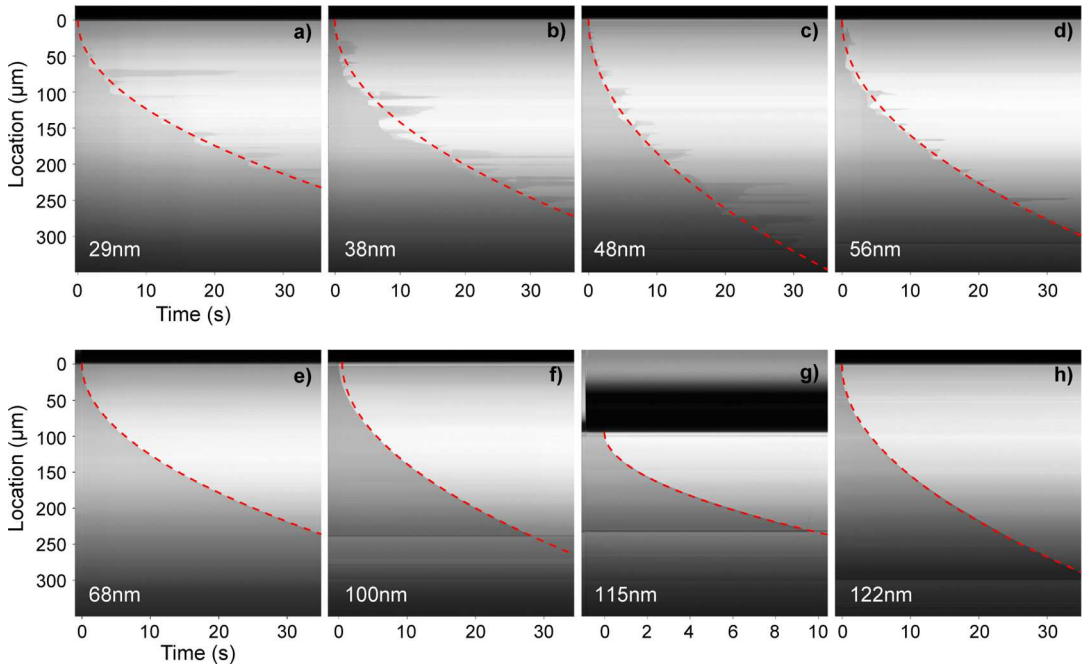

Figure 3. Spatiotemporal diagrams for nanochannels with different heights. The height of channel is marked at the bottom left corner of each subfigure: (a) 29 nm (b) 38 nm (c) 48 nm (d) 56 nm (e) 68 nm (f) 100 nm (g) 115 nm (h) 122 nm. The red dash line in each subfigure is the best parabolic fit to the meniscus motion.

meniscus motion inside the nanochannel, a high speed camera (PHOTRON FASTCAM Mini UX50) mounted on an optical microscope (OLYMPUS BH2) was used to record the whole drying process.

We discovered two different drying behaviors in these 2-D dead-end nanochannels. Successive snapshots of these two behaviors are presented in Figure 2a,b, respectively. For both images, the open end of nanochannel is located on the left side, and the menisci recede from left to right. Figure 2a shows the drying behavior of a 56 nm-high nanochannel, in which the meniscus in the nanochannel did not recede continuously. Instead, the upper half of nanochannel was dried first and the gas started to invade into the liquid column. After a certain length of gas invasion, the whole width of channel was occupied by purging gas. A short length of the liquid water column (referred to as the liquid bridge later) was thus separated from the rest of the water. This liquid bridge served as a barrier for water transport from the apparent meniscus to the open end of channel. After the formation of a liquid bridge, the receding speed of the apparent meniscus started to decrease. This can be explained by the gap between liquid bridge and apparent meniscus, which was filled with saturated water vapor. Under such a condition, evaporation at the apparent meniscus was impeded, and the liquid bridge became the new evaporation front. As a result, the liquid bridge continuously shrunk right after its formation. After the liquid bridge was completely dried, the apparent meniscus resumed its receding toward the dead end of the channel until a new liquid bridge was formed. (Supporting Video 1)

This drying process associated with liquid bridge formation and discontinuous meniscus receding was observed in all nanochannels with heights of 29, 38, 48, and 56 nm. However, this phenomenon was not observed in higher nanochannels. Figure 2b presents the typical drying behavior of a 115 nm-high nanochannel. It can be clearly seen that the meniscus in this nanochannel is sharp, and it moves continuously toward the dead end of the nanochannel. No liquid bridge was observed during the whole drying process. (Supporting Video 2)

To identify the origin of the discontinuous meniscus receding, we repeated the drying experiments for all the 56 nm-high nanochannels for five times and found that discontinuous meniscus receding always occurred in these channels. Although positions of the liquid bridges varied from channel to channel, for the same channel, the liquid bridges always occurred at the same position(s) in every run of the experiment. In addition, the size and the shrinking speed of each liquid bridge also remained the same for all repeated experiments.

Thus, we attribute the formation of liquid bridge in the shallower nanochannels to the surface defects and/or uneven edges introduced during nanochannel fabrication. During the drying (meniscus receding) process, these local surfaces defects can serve as distortion sources. When the receding meniscus passes a defect, the meniscus is distorted from its original shape to achieve lower free energy. This led to the gas invasion into part of the liquid column and eventually the formation of the liquid bridge. For higher nanochannels, the surface defects can also distort the meniscus during the drying process (See Supporting Video 2 for more details). However, due to the relatively low profile of the surface defects, such distortion effect becomes less apparent and will not lead to gas invasion into the liquid column and the break of the meniscus. Therefore, the menisci in these nanochannels receded continuously without formation of liquid bridge.

To further investigate the drying kinetics, successive snapshots of nanochannels are stacked together to generate spatiotemporal diagrams using a MATLAB image processing program. Figure 3a–h reveals the representative drying curves for nanochannels with eight different heights. The darker area indicates that the channel area is filled with water, while the brighter area indicates that the channel area is dry. The black bar on top of each diagrams represents the open end of the

DOI: 10.1021/acs.langmuir.7b02027
Langmuir 2017, 33, 8395–8403

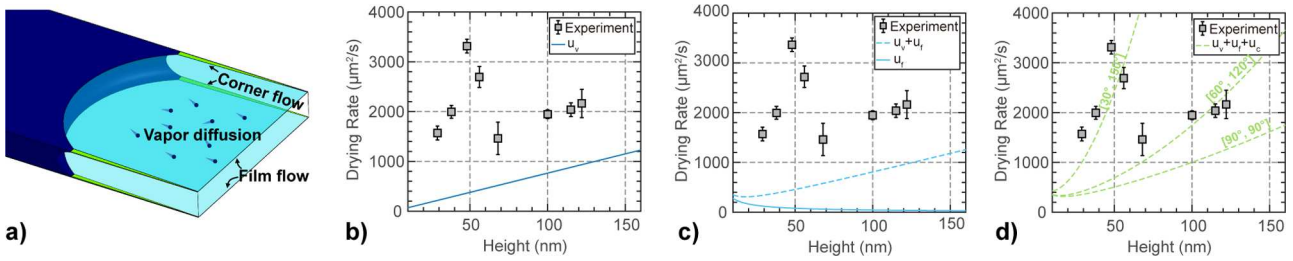

Figure 4. Kinetics of the drying process and the modeling results. (a) Three mechanisms contributing to the drying in the nanochannel: vapor diffusion, thin film flow, and corner flow. (b–d) Experimental and modeling results of the drying rates in channels with different heights.

nanochannel (microchannel area), where the purging gas is introduced to remove the evaporated water vapor. The dead end of the nanochannel can only be seen in some of the diagrams (Figure 3f–h) due to the limited size of field of view.

Clearly, there are two types of drying diagrams, corresponding to the two aforementioned drying behaviors for all nanochannels being investigated. Nanochannels with the discontinuous meniscus receding behavior exhibited rough vapor/liquid interface on spatiotemporal diagrams with a few water spikes. Each of these spikes corresponds to the formation and disappearance of one water bridge in front of the apparent meniscus. By contrast, nanochannels with the continuous meniscus receding behavior exhibited smooth vapor/liquid interface on the diagrams. Obviously, in these nanochannels, the water drying speed is equal to the meniscus receding speed. Since the resistance of water transport R (both vapor phase and liquid phase) is proportional to the meniscus receding length L from the position of meniscus to the open-end of the nanochannel, it is expected that the meniscus receding speed v ($v = \frac{dL}{dt} \propto \frac{1}{R}$) would continuously decrease as the meniscus moves further into the nanochannel. Consequently, the meniscus receding length should follow a square root of time function ($L \propto t^{1/2}$). We thus used the square root functions to fit all drying diagrams and plotted the best fitting curves in Figure 3. Not surprisingly, the menisci motions for deeper nanochannels (68, 100, 115, and 122 nm) perfectly match the fitting drying curves and a constant drying rate, defined as $u = \frac{L^2}{t}$, can be calculated for each channel.[20] However, quite unexpectedly, the menisci motions for the channels with discontinuous meniscus receding also show good matches to square root of time fitting curves, indicating that the intermittent presence of water bridges did not significantly affect the fundamental mechanism(s) of the drying kinetics. As a result, constant drying rates can also be calculated for these channels.

We extract the drying rate from more than 20 nanochannels for each channel height and plot the height dependence in Figure 4. The extracted drying rate ranges from 1500 to 3500 $\mu m^2/s$ and is highly geometric-dependent. It has been reported that the water drying rate inside the nanochannel can be contributed from three different mechanisms: vapor diffusion, thin film flow and corner flow (Figure 4a).[20] Vapor diffusion refers to the process in which water molecules vaporize from the liquid–vapor interface and subsequently diffuse out of the nanochannel. Thin film flow and corner flow refer to two different liquid pathways from the apparent meniscus to the open end of the nanochannel. Due to the significance of van der Waals force in nanoscale, a thin film of liquid water would appear on the inner wall of the vapor-filled channel. In addition, the corner area in noncylindrical channel can also hold liquid water based on the hydrophilicity of inner surfaces. The liquid water on surfaces and corners can extend all the way to the open end of the nanochannel and thus function as alternative pathways for water removal. As a result, the overall drying rate can be described as the sum of the drying rates induced by these three mechanisms.

$$u = u_v + u_f + u_c \tag{1}$$

Here, u_v, u_f, and u_c represent the drying rate induced by vapor diffusion, thin film flow and corner flow, respectively. The analytical expression and the corresponding quantitative contribution of each mechanism are discussed in the following paragraphs. Details of derivation can be found in the Supporting Information.

Vapor Diffusion. The drying rate induced from vapor diffusion u_v can be written as

$$u_v = \frac{2DV_w}{RT}(p_m - p_e) \tag{2}$$

Here, D is the overall vapor diffusivity, V_w is molar volume of water, R is gas constant, and T is temperature. p_m and p_e correspond to the water vapor pressure at the position of meniscus and the open end of the nanochannel. Since the height of our nanochannels ranges from 29 to 122 nm and the mean free path at atmosphere λ is ~70 nm, the Knudsen number ($Kn = \lambda/h$) ranges from ~0.6 to ~2.4, and the water vapor diffusion falls into the transitional regime between pure molecular diffusion and Knudsen diffusion. Therefore, the overall vapor diffusivity should be contributed by both molecular diffusivity D_{AB} and Knudsen diffusivity D_{KN}. However, according to our control experiments performed in a vacuum chamber (see Supporting Information), the contribution from the molecular diffusivity to the overall diffusivity is negligible, and the overall vapor diffusivity is thus roughly equal to the Knudsen diffusivity, which can be expressed as $D_{KN} = \frac{h}{3}\sqrt{\frac{8RT}{\pi M_w}}$ based on the classic Knudsen theory.[22]

Figure 4b shows the effective drying rate of vapor diffusion predicted by eq 2. For comparison, the drying rate extracted from our experimental study for nanochannels with different heights is shown in Figure 4b as well. Obviously, the experimental drying rate (1500–3500 $\mu m^2/s$) is much higher than the theoretical estimation from vapor diffusion. It also shows a complicated channel height dependence compared with the simple monotonic increasing trend of the theoretical estimation. Therefore, other mechanisms should be accounted for better explanation of the experimental results.

Thin Film Flow. The drying rate induced from thin film flow u_f can be written as

DOI: 10.1021/acs.langmuir.7b02027
Langmuir 2017, 33, 8395–8403

$$u_f = -\frac{4A_h}{18\pi h\eta}\ln\left(\frac{\Psi_e}{\Psi_m}\right) \quad (3)$$

where η is viscosity of water, A_h is the Hamaker constant, and ψ_m and ψ_e represent the water chemical potential at the receding meniscus and channel exit, respectively. In this equation, ψ_m can be calculated based on the Young−Laplace equation:

$$\Psi_m = -\frac{2\gamma\cos\theta}{h} \quad (4)$$

where γ is surface tension of water and θ is the contact angle. The negative sign in eq 4 denotes the concave shape of the meniscus. ψ_e is related to the local partial vapor pressure:

$$\Psi_e = \frac{RT}{V_w}\ln\left(\frac{p_e}{p_{sat}}\right) \quad (5)$$

where p_e is the partial water vapor pressure at the exit of nanochannel, and p_{sat} is the saturated water vapor pressure. In our case, the water vapor at the exit of nanochannel is being constantly purged by the nitrogen gas, where the relative humidity (RH = p_e/p_{sat}) is measured to be close to 1%.

It is worth noting that the thickness of thin film on silica surface is calculated based on the Lifshitz theory of van der Waals forces,[23−26] and the Hamaker constant A_h we used is -1.01×10^{-20} J.[26,27] Due to this relatively weak van der Waals force between water and silica surfaces compared with those between water and metal surfaces, the thickness of water thin film in our nanochannel is very limited. For a better illustration, Figure 4c presents the theoretical drying rate induced by thin film flow as well as by both vapor diffusion and thin film flow. It is evident that the drying rate caused by thin film flow is significantly smaller than that caused by vapor diffusion and stronger thin film flow contribution is observed in shallower channels due to their smaller cross-section areas, although thicker thin films are expected in the higher nanochannels.

Corner Flow. The drying rate induced from corner flow u_c can be written as

$$u_c = \frac{2\gamma^4}{3wh\eta}\left(\frac{1}{\Psi_e^3} - \frac{1}{\Psi_m^3}\right)\sum_i \frac{1}{\beta_i}\left(\frac{1}{\tan\frac{\alpha_i}{2}} - \frac{\pi}{2} + \frac{\alpha_i}{2}\right) \quad (6)$$

where α_i is the angle for corner i of channel cross-section, β_i is the "dimensionless flow resistance" parameter for the corresponding corner i, which is only dependent on α_i.[28] The magnitude of corner flow is strongly determined by the corner angle α_i and the related dimensionless flow resistance parameter β_i. For instance, the amount of water a 30° corner can hold is 10 times more than that of a 90° corner. Therefore, slight change in corner angle could make huge impact on the corner flow contribution to the drying rate. Figure 4d presents the sum of the theoretical drying rates induced by all three aforementioned mechanisms. With the drying rate contribution by vapor diffusion and thin film flow fixed, three different cross-section profiles are selected to calculate the corresponding theoretical drying rate contributed by corner flow: (1) rectangle cross-section with four corners as [90°, 90°, 90°, 90°]; (2) trapezoid cross-section with four corners as [60°, 60°, 120°, 120°]; (3) trapezoid cross-section with four corners as [30°, 30°, 150°, 150°]. Clearly, the corner flow-induced drying rate increases monotonically with the increasing channel height for a specified cross-section profile, and there are significant differences of the theoretical drying rates among three cross-section profiles. Therefore, accurate measurement of the corner angles of nanochannels is required to quantify the corner flow contribution. We characterized the surface profile of our open nanochannel with AFM and typical results are exhibited in Figure 5a. Due to the imperfect fabrication, the sidewall of our

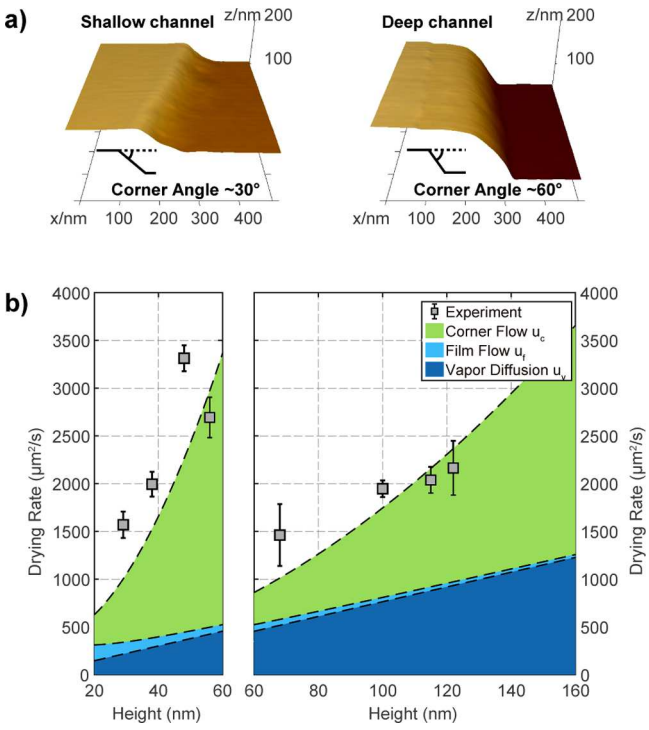

Figure 5. Characterization of the corners of channel cross-section and corresponding impact to the drying rate of channels with different heights. (a) Sidewall characterization of open nanochannels with AFM. Shallow channels (29−56 nm) have corner angles around 30°. Deep channels (68−122 nm) have corner angles around 60°. (b) Experimental and modeling results of the drying rates in channels with different heights.

nanochannel is not vertical (see Supporting Information). Based on our measurement, our shallow channels (29−56 nm) show inclined sidewall with the corner angle around α_i = 30°, 150°. The corner angles of our deeper channels (68 nm −122 nm) are around α_i = 60°, 120°. This proves that the nonmonotonic dependence of our experimental drying rates on channel height originates from the existence of two different corner angles. After consideration of the corrected corner flow in our fabricated nanochannels, theoretical drying rates for different channel heights are calculated, and the contributions from vapor diffusion, thin film flow, and corner flow are replotted in Figure 5b.

While the theoretical prediction qualitatively shows the same trend with the experimental results, there are still quantitative differences between the experimental results and theoretical predictions. Such difference may result from different corner flow contribution due to slight difference of corner angles from nanochannel to nanochannel or different vapor diffusivity. The second reason is of great importance to investigate since water vapor diffusion in nanoconfinement has not been accurately measured experimentally, and it is not clear if it actually can be described by the classic Knudsen theory.[29] In fact, in Knudsen's

DOI: 10.1021/acs.langmuir.7b02027
Langmuir 2017, 33, 8395−8403

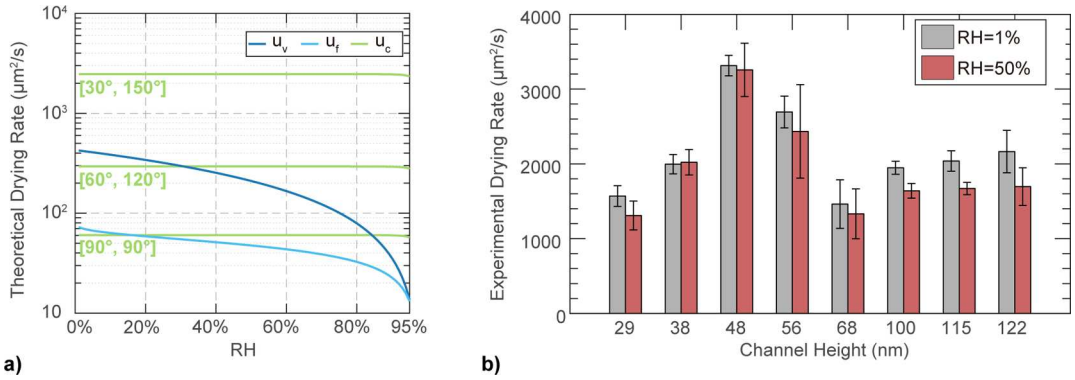

Figure 6. Relative humidity-dependent study of drying rates in nanochannels. (a) Theoretical estimation of drying rates in 56 nm-high nanochannel. Contributions from three different mechanisms are plotted separately. (b) Experimental drying rate measurements of nanochannels with different height. RH = 1% stands for the experiments with dry nitrogen purging. RH = 50% stands for the experiments without purging. At least 15 experiments have been done for each data group.

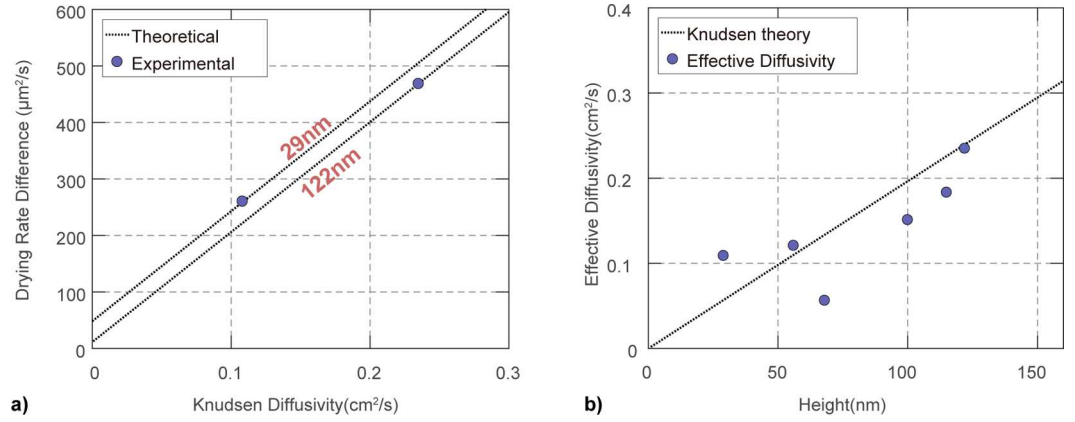

Figure 7. Correlation of drying rate difference between 1% and 50% experiment with effective Knudsen diffusivity and channel heights. (a) Theoretical correlation between drying rate difference and Knudsen diffusivity for 29 nm-high and 122 nm-high channels. Experimental values are used to calculate the effective Knudsen diffusivity. (b) Experimentally extracted effective Knudsen diffusivity at different channel heights. (29 nm, 56 nm, 68 nm, 100 nm, 115 nm, 122 nm).

original theory, the hypothesis of hard-sphere noninteracting gas and hard wall has been made, and the collision between gas molecule and wall surface is completely diffusive.[22] Despite this simple hypothesis, Knudsen's theory showed good agreement with various gas transport experiments in microscale confinement[22,30,31] and has been widely used for transport analysis in porous structures for decades.[32,33] However, recent theoretical[34−37] and experimental work[9,10,38−40] shows the deviation of Knudsen's formula under stringent confinement, where gas−wall interaction is significant and can strongly affect the gas transport inside nanoscale conduits. Latest research in graphitic nanoconduits (carbon nanotube, graphene oxide membrane) reported enhanced gas diffusivity inside, suggesting that the gas−wall collision could be specular.[9,10] In this scenario, the tangential molecular momentum before and after collision is preserved and a higher Knudsen diffusivity (for H_2, He, Ne, O_2, Ar, N_2, etc.) should be expected. On the other hand, for nanochannels of which surfaces with strong physical adsorption, the gas transport inside is hindered as the kinetic energy of gas molecule is not enough to escape from the attraction field of the channel inner surfaces. Experiments in microporous silica structures have proven the deviation of Knudsen's model, and significantly lower Knudsen diffusivities (for CO_2, C_2H_4, C_2H_6) have been measured.[38,41,42]

In order to check whether water vapor diffusivity is greater or less than the classic Knudsen diffusivity, it is necessary to completely decouple water vapor transport with water liquid transport in nanoconfined spaces (e.g., due to capillary condensation), which is actually the major challenge that prevented accurate estimation of water vapor diffusion in previous investigations (based on pressure-driven or humidity-gradient driven vapor transport).[43−45] This problem can be resolved in our drying experiments as liquid and vapor transport have different dependence on ambient humidity and/or drastically different contributions to overall water transport. Figure 6a reveals the theoretical drying rates of vapor diffusion (u_v), thin film flow (u_f), and corner flow (u_c) as a function of the relative humidity at the exit of the nanochannel. Based on our model, while the drying rates induced by vapor diffusion (u_v) and thin film flow (u_f) show strong dependence on the relative humidity, the drying rate induced by corner flow (u_c) remains independent to relative humidity over a large range no matter what the corner angles are. What's more, the drying rate induced by vapor diffusion u_v is about 1 order of magnitude higher than the drying rate induced by thin film flow. Based on these two observations, the vapor transport and two liquid transport can be successfully decoupled if the drying experiments are performed at an ambient humidity different from our previous experiments (RH

DOI: 10.1021/acs.langmuir.7b02027
Langmuir 2017, 33, 8395−8403

~ 1%). To achieve that, we placed the chip in the environment with RH = 50%, and no purging nitrogen was introduced into the reservoir. The relative humidity at the open end of nanochannel can be considered as 50% due to negligible diffusion resistance of reservoir and microchannel. The measured drying rates for channels with different heights are shown in Figure 6b as "RH = 50%". For comparison, nitrogen gas purging results are shown as "RH = 1%".

Clearly, there are statistical differences between the measured drying rates at these two different RHs for most of the nanochannels except for 38 nm-high and 48 nm-high nanochannels, indicating that these nanochannels have very sharp corners and the contribution from corner flow to water drying is significantly larger than the other two.

For all other nanochannels, the drying rates from high RH (50%) experiments are lower than those from low RH (1%) experiments. The differences between these two drying rates correspond to the change of vapor diffusion (u_v) and thin film flow (u_f) since the corner flow contributions (u_c) are independent of ambient RH.

$$\Delta u = \Delta(u_v + u_f) \tag{7}$$

Thus, the significant contribution from corner flow to the overall drying rate can be excluded without knowing the exact corner angles, which leads us to more accurate investigation of water vapor diffusivity. Figure 7a shows how theoretical drying rate difference is related to the water vapor diffusivities at different channel heights (29 and 122 nm). Experimental results are also presented in Figure 7a, and the effective diffusivity corresponding to each channel height can be therefore extracted. According to our calculation, the effective water vapor diffusivity inside silica nanochannels ranges from 0.055 cm^2/s to 0.235 cm^2/s in a height range of 29 nm −122 nm, as exhibited in Figure 7b. Our results suggest that Knudsen's theory can roughly describe water vapor diffusivity, despite strong adsorption between water molecules and silica surface.

The agreement between extracted effective water vapor diffusivity and Knudsen's theory is likely a result of both strong physical adsorption and specular gas-wall collision. For gases with strong affinity to solids, the gas−solid interaction can affect the gas molecule trajectories under nanoconfinement and the corresponding gas diffusivity is expected to deviate from classic Knudsen's theory.[29] On the other hand, as proposed by Lei et al., the water molecule adsorption on to the silica surface can alter the tangential momentum accommodation coefficient (TMAC), which is related to gas-wall collision inside nanochannels.[46] Previous studies have shown that the first adsorption of water molecules to surfaces can reorient themselves into ordered layers.[47−49] This "ice-like" configuration can fill the surface depressions and induce a smooth surface for more specular collision. Although this validity requires further investigation, our effective diffusivity measurement sheds lights on the water vapor transport in nanoscale conduits and nanoporous media.

CONCLUSION

In conclusion, planar nanofluidic devices were successfully made to study water drying in the dead-end nanochannels. Two different drying behaviors, i.e., continuous meniscus receding and discontinuous meniscus receding due to liquid bridge formation/vaporization ahead of the meniscus, were observed in these nanochannels, although both of them led to constant drying rates. We accurately measured drying rates inside the channels with different geometries. Vapor diffusion, thin film flow, and corner flow are proposed to quantitatively explain the experimental drying rates from different channels. Our results show that corner flow and vapor diffusion are the two major contributors to liquid drying in nanoconfinements with feature size larger than 20 nm. Our results also show that water vapor diffusivity inside silica nanochannels can be described by classic Knudsen theory despite strong affinity of water vapor. These findings provide new insights of liquid drying and vapor transport in nanoscale confined spaces, which will elucidate many related processes occurring in nature and industry and improve corresponding applications.

METHODS

The dead-end nanochannel device is composed of two substrates: (1) silicon substrate with 30 open parallel nanochannels and (2) glass substrate with one microchannel and two reservoirs. Both substrates are 500-μm thick. The fabrication of the silicon substrate started from transferring nanochannel patterns (L: 1000 μm, W: 3 μm) from chrome photomask to photoresist (S1813) with photolithography. The nanochannels were then being etched with a reactive ion etching system (Plasma-Therm 790). The etch rate had been adjusted to ~1 Å/s for accurate control of nanochannel height. Afterward, the silicon substrate was cleaned with piranha solution (H_2O_2:H_2SO_4 = 1:3) and kept in a furnace at 1000 °C to grow 300 nm-thick thermal oxide. The fabrication of the glass substrate started with polysilicon deposition on to the plain glass substrate. 500 nm-thick polysilicon was deposited on both side of the glass substrate in a furnace via chemical vapor deposition (CVD). With the help of photolithography, reservoir patterns were defined and aligned on the photoresist layer spun on both sides of the substrate. Exposed polysilicon on both sides was then etched away by reactive ion etch (RIE). Subsequently, 49% hydrofluoric acid (HF) was used to etch through the glass substrate with the patterned polysilicon as etching mask. Similarly, photolithography and RIE were used to create microchannel patterns on the polysilicon layer, bridging the neighboring reservoirs. The microchannel was also etched by 49% HF, and the depth was around 100 μm. Afterward, the polysilicon layer was removed by tetramethylammonium hydroxide (TMAH). The two substrates were cleaned with piranha solution before being bonded together through anodic bonding technique. The bonding process was carried out under a voltage of 500 V at 400 °C with our homemade bonding setup.

ASSOCIATED CONTENT

Supporting Information

The Supporting Information is available free of charge on the ACS Publications website at DOI: 10.1021/acs.langmuir.7b02027.

Water chemical potential; detailed derivation of drying rates u_v, u_f, and u_c; effects of thermal oxidation on nanochannels geometry; and drying experiments under vacuum. (PDF)

Supporting video 1 (AVI)

Supporting video 2 (AVI)

AUTHOR INFORMATION

Corresponding Author

*E-mail: duan@bu.edu.

ORCID

Quan Xie: 0000-0002-4670-6899

Siyang Xiao: 0000-0003-0658-0811

Chuanhua Duan: 0000-0002-5453-5321

DOI: 10.1021/acs.langmuir.7b02027
Langmuir 2017, 33, 8395−8403

Notes

The authors declare no competing financial interest.

■ ACKNOWLEDGMENTS

This work is supported by the Faculty Startup Fund (Boston University, USA) and the NSF Faculty Early Career Development (CAREER) Program award (CBET − 1653767). The authors would like to thank the Photonics Center at Boston University for the use of their fabrication and characterization facilities.

■ REFERENCES

(1) Luikov, A. V. Heat and Mass Transfer in Capillary-Porous Bodies. In *Advances in Heat Transfer*; Thomas, F. I., James, P. H., Eds;. Elsevier: Amsterdam, 1964; Vol. *1*, pp 123−184.

(2) Whitaker, S. Coupled Transport in Multiphase Systems: A Theory of Drying. In *Advances in Heat Transfer*, Hartnett, J. P., Irvine, T. F., Cho, Y. I., Greene, G. A., Eds.; Elsevier: Amsterdam, 1998; Vol. *31*, pp 1−104.

(3) GURR, C. G.; MARSHALL, T. J.; HUTTON, J. T. MOVEMENT OF WATER IN SOIL DUE TO A TEMPERATURE GRADIENT. *Soil Sci.* **1952**, *74* (5), 335−346.

(4) Taylor, S. A.; Cavazza, L. The Movement of Soil Moisture in Response to Temperature Gradients. *Soil Sci. Soc. Am. J.* **1954**, *18* (4), 351−358.

(5) Laurindo, J. B.; Prat, M. Numerical and experimental network study of evaporation in capillary porous media. Drying rates. *Chem. Eng. Sci.* **1998**, *53* (12), 2257−2269.

(6) Shokri, N.; Lehmann, P.; Or, D. Critical evaluation of enhancement factors for vapor transport through unsaturated porous media. *Water Resour. Res.* **2009**, *45* (10), W10433.

(7) Yiotis, A. G.; Boudouvis, A. G.; Stubos, A. K.; Tsimpanogiannis, I. N.; Yortsos, Y. C. Effect of liquid films on the drying of porous media. *AIChE J.* **2004**, *50* (11), 2721−2737.

(8) Prat, M. On the influence of pore shape, contact angle and film flows on drying of capillary porous media. *Int. J. Heat Mass Transfer* **2007**, *50* (7−8), 1455−1468.

(9) Holt, J. K.; Park, H. G.; Wang, Y.; Stadermann, M.; Artyukhin, A. B.; Grigoropoulos, C. P.; Noy, A.; Bakajin, O. Fast Mass Transport Through Sub-2-Nanometer Carbon Nanotubes. *Science* **2006**, *312* (5776), 1034.

(10) Hinds, B. J.; Chopra, N.; Rantell, T.; Andrews, R.; Gavalas, V.; Bachas, L. G. Aligned Multiwalled Carbon Nanotube Membranes. *Science* **2004**, *303* (5654), 62.

(11) Duan, C.; Wang, W.; Xie, Q. Review article: Fabrication of nanofluidic devices. *Biomicrofluidics* **2013**, *7* (2), 026501.

(12) Stein, D.; Kruithof, M.; Dekker, C. Surface-Charge-Governed Ion Transport in Nanofluidic Channels. *Phys. Rev. Lett.* **2004**, *93* (3), 035901.

(13) Duan, C.; Majumdar, A. Anomalous ion transport in 2-nm hydrophilic nanochannels. *Nat. Nanotechnol.* **2010**, *5* (12), 848−852.

(14) Xie, Q.; Xin, F.; Park, H. G.; Duan, C. Ion transport in graphene nanofluidic channels. *Nanoscale* **2016**, *8* (47), 19527−19535.

(15) Karnik, R.; Duan, C.; Castelino, K.; Daiguji, H.; Majumdar, A. Rectification of Ionic Current in a Nanofluidic Diode. *Nano Lett.* **2007**, *7* (3), 547−551.

(16) Vlassiouk, I.; Siwy, Z. S. Nanofluidic Diode. *Nano Lett.* **2007**, *7* (3), 552−556.

(17) Cheng, L.-J.; Guo, L. J. Nanofluidic diodes. *Chem. Soc. Rev.* **2010**, *39* (3), 923−938.

(18) Duan, C.; Karnik, R.; Lu, M.-C.; Majumdar, A. Evaporation-induced cavitation in nanofluidic channels. *Proc. Natl. Acad. Sci. U. S. A.* **2012**, *109* (10), 3688−3693.

(19) Zhong, J.; Zandavi, S. H.; Li, H.; Bao, B.; Persad, A. H.; Mostowfi, F.; Sinton, D. Condensation in One-Dimensional Dead-End Nanochannels. *ACS Nano* **2017**, *11* (1), 304−313.

(20) Eijkel, J. C. T.; Dan, B.; Reemeijer, H. W.; Hermes, D. C.; Bomer, J. G.; van den Berg, A. Strongly Accelerated and Humidity-Independent Drying of Nanochannels Induced by Sharp Corners. *Phys. Rev. Lett.* **2005**, *95* (25), 256107.

(21) Phan, V.-N.; Nguyen, N.-T.; Yang, C.; Joseph, P.; Gué, A.-M. Fabrication and Experimental Characterization of Nanochannels. *J. Heat Transfer* **2012**, *134* (5), 051012−051012−6.

(22) Knudsen, M. Die Gesetze der Molekularströmung und der inneren Reibungsströmung der Gase durch Röhren. *Ann. Phys. (Berlin, Ger.)* **1909**, *333* (1), 75−130.

(23) Hamaker, H. C. The London—van der Waals attraction between spherical particles. *Physica* **1937**, *4* (10), 1058−1072.

(24) Dzyaloshinskii, I. E.; Lifshitz, E. M.; Pitaevskii, L. P. GENERAL THEORY OF VAN DER WAALS' FORCES. *Soviet Physics Uspekhi* **1961**, *4* (2), 153.

(25) Hough, D. B.; White, L. R. The calculation of hamaker constants from liftshitz theory with applications to wetting phenomena. *Adv. Colloid Interface Sci.* **1980**, *14* (1), 3−41.

(26) Israelachvili, J. N. *Intermolecular and Surface Forces*, 3rd ed.; Academic Press: London, 2010.

(27) Hirasaki, G. J. Wettability: Fundamentals and Surface Forces. *SPE Form. Eval.* **1991**, *6*, 217−226.

(28) Ransohoff, T. C.; Radke, C. J. Laminar flow of a wetting liquid along the corners of a predominantly gas-occupied noncircular pore. *J. Colloid Interface Sci.* **1988**, *121* (2), 392−401.

(29) Bhatia, S. K.; Bonilla, M. R.; Nicholson, D. Molecular transport in nanopores: a theoretical perspective. *Phys. Chem. Chem. Phys.* **2011**, *13* (34), 15350−15383.

(30) Knudsen, M.; Fisher, W. J. The Molecular and the Frictional Flow of Gases in Tubes. *Physical Review (Series I)* **1910**, *31* (5), 586−588.

(31) Steckelmacher, W. Knudsen flow 75 years on: the current state of the art for flow of rarefied gases in tubes and systems. *Rep. Prog. Phys.* **1986**, *49* (10), 1083.

(32) Cunningham, R. E.; Williams, R. J. J. *Diffusion in Gases and Porous Media*; Plenum Press: New York, 1980.

(33) Jackson, R. *Transport in Porous Catalysts*; Elsevier Scientific Pub. Co.: Amsterdam/New York, 1977.

(34) Skoulidas, A. I.; Ackerman, D. M.; Johnson, J. K.; Sholl, D. S. Rapid Transport of Gases in Carbon Nanotubes. *Phys. Rev. Lett.* **2002**, *89* (18), 185901.

(35) Sokhan, V. P.; Nicholson, D.; Quirke, N. Fluid flow in nanopores: Accurate boundary conditions for carbon nanotubes. *J. Chem. Phys.* **2002**, *117* (18), 8531−8539.

(36) Bhatia, S. K.; Nicholson, D. Anomalous transport in molecularly confined spaces. *J. Chem. Phys.* **2007**, *127* (12), 124701.

(37) Bhatia, S. K.; Nicholson, D. Hydrodynamic Origin of Diffusion in Nanopores. *Phys. Rev. Lett.* **2003**, *90* (1), 016105.

(38) Qiao, S. Z.; Bhatia, S. K. Diffusion of n-decane in mesoporous MCM-41 silicas. *Microporous Mesoporous Mater.* **2005**, *86* (1−3), 112−123.

(39) Qiao, S. Z.; Bhatia, S. K. Diffusion of Linear Paraffins in Nanoporous Silica. *Ind. Eng. Chem. Res.* **2005**, *44* (16), 6477−6484.

(40) Huang, Q.; Qamar, R. A.; Eić, M. Single component and binary diffusion of n-heptane and toluene in SBA-15 materials. *Adsorption* **2011**, *17* (1), 27−38.

(41) Alsyouri, H. M.; Lin, J. Y. S. Gas Diffusion and Microstructural Properties of Ordered Mesoporous Silica Fibers. *J. Phys. Chem. B* **2005**, *109* (28), 13623−13629.

(42) Chong, S.-S.; Jobic, H.; Plazanet, M.; Sholl, D. S. Concentration dependence of transport diffusion of ethane in silicalite: A comparison between neutron scattering experiments and atomically detailed simulations. *Chem. Phys. Lett.* **2005**, *408* (1−3), 157−161.

(43) Shui, L.; Eijkel, J. C. T.; van den Berg, A. Multiphase flow in micro- and nanochannels. *Sens. Actuators, B* **2007**, *121* (1), 263−276.

(44) Petukhov, D. I.; Berekchiian, M. V.; Pyatkov, E. S.; Solntsev, K. A.; Eliseev, A. A. Experimental and Theoretical Study of Enhanced Vapor Transport through Nanochannels of Anodic Alumina Membranes in a Capillary Condensation Regime. *J. Phys. Chem. C* **2016**, *120* (20), 10982−10990.

DOI: 10.1021/acs.langmuir.7b02027
Langmuir 2017, 33, 8395−8403

(45) Lei, W.; Fong, N.; Yin, Y.; Svehla, M.; McKenzie, D. R. Science of Water Leaks: Validated Theory for Moisture Flow in Microchannels and Nanochannels. *Langmuir* **2015**, *31* (42), 11740−11747.
(46) Lei, W.; McKenzie, D. R. Enhanced Water Vapor Flow in Silica Microchannels: The Effect of Adsorbed Water on Tangential Momentum Accommodation. *J. Phys. Chem. C* **2015**, *119* (38), 22072−22079.
(47) Alibakhshi, M. A.; Xie, Q.; Li, Y.; Duan, C. Accurate measurement of liquid transport through nanoscale conduits. *Sci. Rep.* **2016**, *6*, 24936.
(48) Asay, D. B.; Kim, S. H. Evolution of the Adsorbed Water Layer Structure on Silicon Oxide at Room Temperature. *J. Phys. Chem. B* **2005**, *109* (35), 16760−16763.
(49) Li, T.-D.; Gao, J.; Szoszkiewicz, R.; Landman, U.; Riedo, E. Structured and viscous water in subnanometer gaps. *Phys. Rev. B: Condens. Matter Mater. Phys.* **2007**, *75* (11), 115415.

DOI: 10.1021/acs.langmuir.7b02027
Langmuir 2017, 33, 8395−8403